Least-Squares Triple Cross-Wavelet and Multivariate Regression Analyses of Climate and River Flow in the Athabasca River Basin

EBRAHIM GHADERPOUR[,a] MOHAMED SHERIF ZAGHLOUL,[a] HATEF DASTOUR,[a] ANIL GUPTA,[b] GOPAL ACHARI,[a] AND QUAZI K. HASSAN[a]

[a] *Schulich School of Engineering, University of Calgary, Calgary, Alberta, Canada*
[b] *Resource Stewardship Division, Alberta Environment and Protection Areas, University Research Park, Calgary, Alberta, Canada*

ABSTRACT: River flow monitoring is a critical task for land management, agriculture, fishery, industry, and other concerns. Herein, a robust least squares triple cross-wavelet analysis is proposed to investigate possible relationships between river flow, temperature, and precipitation in the time–frequency domain. The Athabasca River basin (ARB) in Canada is selected as a case study to investigate such relationships. The historical climate and river flow datasets since 1950 for three homogeneous subregions of the ARB were analyzed using a traditional multivariate regression model and the proposed wavelet analysis. The highest Pearson correlation (0.87) was estimated between all the monthly averaged river flow, temperature, and accumulated precipitation for the subregion between Hinton and Athabasca. The highest and lowest correlations between climate and river flow were found to be during the open warm season and cold season, respectively. Particularly, the highest correlations between temperature, precipitation, and river flow were in May (0.78) for Hinton, July (0.54) for Athabasca, and September (0.44) for Fort McMurray. The new wavelet analysis revealed significant coherency between annual cycles of climate and river flow for the three subregions, with the highest of 33.7% for Fort McMurray and the lowest of 4.7% for Hinton with more coherency since 1991. The phase delay analysis showed that annual and semiannual cycles of precipitation generally led the ones in river flow by a few weeks mainly for the upper and middle ARB since 1991. The climate and river flow anomalies were also demonstrated using the baseline period 1961–90, showing a significant increase in temperature and decrease in precipitation since 1991 for all the three subregions. Unlike the multivariate regression, the proposed wavelet method can analyze any hydrometeorological time series in the time–frequency domain without any need for resampling, interpolation, or gap filling.

KEYWORDS: Algorithms; Data processing/distribution; Remote sensing; Regression analysis; Spectral analysis/models/distribution; Time series

1. Introduction

Maintaining and monitoring water availability in watersheds is crucial for the preservation of the natural ecosystem, livelihood of residents, and industries (Xu and Singh 2004; Wolfe et al. 2005). Climate and land cover change play a significant role in the hydrological behavior of watersheds and can significantly influence the ecology and ecosystem (Kerkhoven et al. 2011; Shrestha et al. 2017; Shah et al. 2020). For example, Morales-Marín et al. (2019) mentioned that increasing river temperature can raise metabolic rates and force fish species to migrate upstream where the water is cooler, or forest fires can significantly damage vegetation canopy and increase runoff after rainfalls or snowmelts (Afrin et al. 2019; Zaghloul et al. 2022). The main parameters affecting hydrology and water availability are temperature, precipitation, land use and land cover (LULC), soil characteristics, and topography (Monk et al. 2012; Eum et al. 2016; Peters et al. 2013, 2022; Belvederesi et al. 2022). In certain basins, particularly in cold climates, study of streamflow influential factors, such as climate and LULC, is very challenging.

Various models have been employed in literature for analyzing streamflow and its influential factors, such as the Soil and Water Assessment Tool (SWAT), bivariate nonparametric estimator, multivariate double logarithm, multivariate regression, and cross-wavelet and wavelet coherence analyses (Shrestha et al. 2017; Pérez Ciria and Chiogna 2020; Ghaderpour et al. 2021; Khan et al. 2022). Wavelet analysis has proven to be very effective for monitoring and prediction of streamflow, vegetation, and climate measurements (Ghaderpour et al. 2021; Dastour et al. 2022). In fact, decomposing a nonstationary time series into the time–frequency domain can reveal the periodic and aperiodic components of time series. Traditional correlation methods, such as Pearson correlation, cannot show the dynamic of measurement dependency over time; however, wavelet coherency analysis can show how measurements are coherent over time and frequency, providing an excellent tool in hydrometeorological studies. Thus far, the cross-wavelet and coherency analyses have been mainly applied to a pair of time series. In the present work, a robust triple cross-wavelet method for simultaneous analysis of three time series is proposed (i.e., river flow, precipitation, and temperature).

Herein, the Athabasca River basin (ARB) is chosen as a case study because it is in a cold climate region whose streamflow is highly sensitive to climate change and has a great

⁂ Denotes content that is immediately available upon publication as open access.

Corresponding author: Quazi K. Hassan, qhassan@ucalgary.ca

importance for the province of Alberta in Canada (Zaghloul et al. 2022). In the present work, a traditional multivariate regression model is applied to show the correlation between river flow, precipitation, and temperature for three subregions of ARB and to compare the results with the triple cross-wavelet analysis. The results presented in this research can be considered as a complement to the results by Ghaderpour et al. (2021), Dastour et al. (2022), and Zaghloul et al. (2022) in that they show how the principal climatic factors (i.e., precipitation and temperature) simultaneously have influenced the river flow of Athabasca River in each calendar month and season, and in the time–frequency domain.

a. Earlier research on the Athabasca River basin

The ARB consists of boreal forests, providing livelihood to indigenous people and a habitat for many wildlife species. Human activities in the ARB include fishing, coal, and oil sand mining, natural gas extraction, agriculture, and pulp and paper production (Afrin et al. 2019; Gillanders et al. 2008). Many studies have been done on the ARB in recent years. Shrestha et al. (2017) utilized the Soil and Water Assessment Tool (SWAT) to evaluate the effect of climate change on water resources and showed that the water resources of the ARB possibly will increase in the future. In another study, Shrestha and Wang (2018) applied SWAT and concluded that the climate influence on soil erosion of the ARB is region-based and LULC dependent. Hwang et al. (2018) used a long-term water balance technique to demonstrate how the river flow downstream of the ARB (e.g., Fort McMurray) is significantly higher than the flow upstream of the ARB (e.g., Hinton). Rood et al. (2015) estimated trends for century-long river flows in the ARB using the linear Pearson correlation and nonparametric Kendall methods. Their results showed an overall decline in annual flow close to the mountainous region (Hinton). Other studies also showed a decline in the Athabasca River flow over the past 70 years (Zhang et al. 2001; Burn and Elnur 2002; Zaghloul et al. 2022). Climate change has resulted in shifting peak spring flows to earlier dates, increased winter streamflow, and decreased summer streamflow (Burn et al. 2004a,b; Eum et al. 2017; Rood et al. 2008; Schindler and Donahue 2006). In addition, a warming trend during the winter and a regime shift from wet to dry in the Palmer drought severity index (PDSI) have been found since 1980 for the Peace–Athabasca delta (Timoney 2021). Previous studies have confirmed that the hydrology of the ARB is changing due to increasing temperatures in the Canadian province of Alberta by studying the observed trends in river flow and climate time series (Peters et al. 2013; Hassan et al. 2021). However, the research gap on how coherent the cycles and quasi-cycles of river flow and climate of ARB are and how much they lead/lag from each other over time and frequency has not yet been filled in the literature.

b. Main contributions

Possible interactions between climate, land cover, and river flow have been studied for three subregions of the ARB, namely the upper, middle, and lower ARB, in several studies (Dibike et al. 2018; Zaghloul et al. 2022; Dastour et al. 2022). In the present study, three major gauging stations along the Athabasca River with long-term historical measurements were selected, namely those at Hinton, at Athabasca, and below Fort McMurray. Then three new subregions were carefully delineated which were different from the subregions in earlier studies mentioned above. The new subregions were delineated according to terrain specific, soil, and LULC types to precisely represent the river flows measured at the three stations mentioned above. The remote sensing–derived LULC measurements for 2001–20 are first analyzed to show how the land cover dynamics may have impacted the river flow over the past two decades. Then, from the gridded hybrid climate dataset, the temperature and precipitation within the new three subregions are calculated by taking their average. Next, the climate and river flow anomalies with respect to a baseline period 1961–90 were derived to show how climate and river flow changed over time with respect to the baseline. Finally, possible impacts of precipitation and temperature change on river flow measured at the three stations since the 1950s are shown via multivariate regression and the proposed triple cross-wavelet analyses. Note that since there was no river flow gauging station downstream after Fort McMurray that could provide long and continuous historical river flow measurements, a part of the ARB in the far lower reach was not considered. However, the readers are referred to Hebert (2019) and Peters et al. (2022), who studied the impact of climate change and human activities on river flow and aquatic birds after Fort McMurray in the lower ARB that experienced a quick oil sands development in recent years. The main contributions of this research are summarized below.

1) A traditional multivariate regression model is applied to monthly derived river flow, precipitation, and temperature measurements for the open warm season, cold season, annual period, and each calendar month.
2) A novel triple cross-wavelet analysis technique is proposed for estimating coherency and phase delay between cycles and quasi-cycles of river flow and climate time series in the time–frequency domain.

The multivariate regression correlation and wavelet coherency, compared in this research, provide a new insight into how climate may have impacted the Athabasca River flow in certain periods. In particular, the triple cross-wavelet analysis can show in which periods the seasonal cycles of river flow and climate are significantly coherent and how much they lead/lag from each other.

2. Materials and methods

a. Study area

The ARB is mostly in the province of Alberta with a small portion in the province of Saskatchewan, Canada. It extends from the Columbia Glacier in the Canadian Rocky Mountains to Lake Athabasca. The drainage area of the
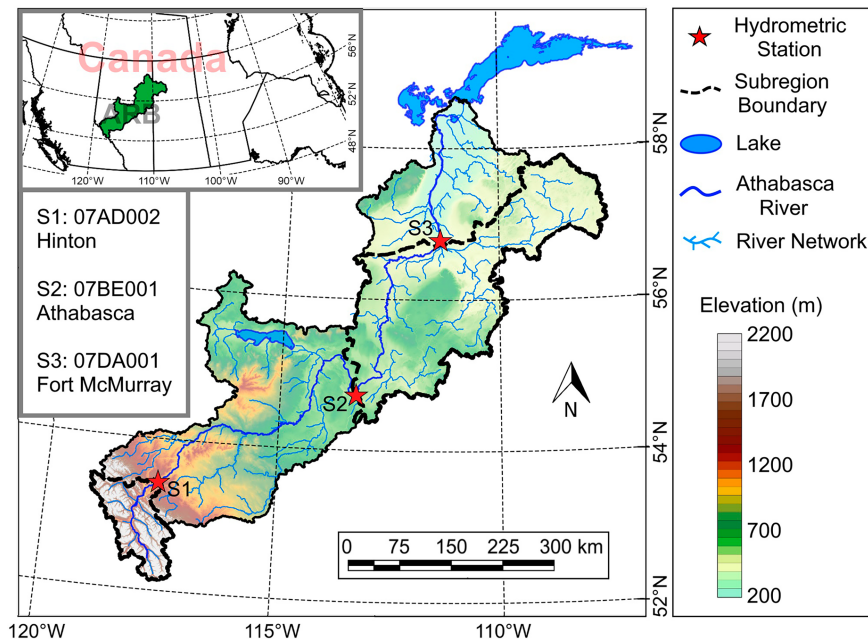
FIG. 1. Map of the ARB showing the boundaries of the subregions and the locations of the gauging stations.

ARB is approximately 138 000 km². The upper region or southern part of the ARB is mountainous with elevations of approximately 1700–2200 m above mean sea level. The following section of the Athabasca River flows through the foothills of the Rocky Mountains with a change of topography between the mountains and the prairies. The rest of the ARB lies in the Canadian Prairies in northeast Alberta and western Saskatchewan (Bawden et al. 2014; Belvederesi et al. 2020a). The climate within the ARB was described to have annual average maximum and minimum temperatures of approximately 6.2° and −5.2°C, respectively. Precipitation was reported to be an average of 492 mm annually (Bawden et al. 2014).

The Athabasca River, inside the ARB, is the largest undammed river in Alberta, Canada. It originates at Columbia Glacier in Jasper National Park and extends about 1300 km toward the northeast of the ARB, and flows to Lake Athabasca, last flowing to the Arctic Ocean (Du et al. 2019). The ARB was divided into four subregions in this study. The first subregion outlet is at Hinton, monitored by the Water Survey of Canada (WSC) station 07AD002. The second subregion is between Hinton and Athabasca, and its river outlet is monitored by WSC station 07BE001 at Athabasca. The third subregion lies between Athabasca and Fort McMurray, monitored by WSC station 07DA001 below Fort McMurray. The final downstream subregion, which lies between Fort McMurray and Lake Athabasca, is monitored by the WSC station 07DD001 at Embarras Airport, excluded here due to very limited measurements (Zaghloul et al. 2022). Figure 1 shows a map of the ARB as well as the subregions and the WSC stations used, where the background digital elevation model is from the Shuttle Radar Topography Mission (SRTM) at 30-m spatial resolution, which

is publicly available at https://earthexplorer.usgs.gov/ (Last accessed on 23 July 2023).

According to the map of Alberta Soil Groups produced by Alberta Agriculture, Food and Rural Development, the main soil groups for the first subregion (before S1) are brunisols and gray luvisols, for the second subregion (between S1 and S2) are gray luvisols and dark gray chernozemics, and for the third subregion (between S2 and S3) are gray luvisols and organics. Brunisols, occurring in the mountainous region, are thin soils (2–15 cm) with a limited frost-free period, and generally not suitable for agriculture. Gray luvisols occur in most parts of the region with mixed forests or in transition zones between grassland and forests where their agricultural capability depends on the amount of organic matter. Dark gray chernozemic soils are formed during transitions between grasslands and forests, and are most suitable for agriculture. Organic soils, also known as peat or fen soils, occurring in wetlands, receive water and nutrients from mineral-rich groundwater or surface water (Frelich and Reich 2010; Lavkulich and Arocena 2011; Hwang et al. 2023).

b. Datasets and preprocessing

In this study, the hybrid climate dataset provided by Alberta Environment and Parks is utilized. This dataset is based on a framework, the Reference Reliability Evaluation System (REFRES), that systematically ranks multiple climate datasets including station-based, multisource, and reanalysis-based datasets to produce the hybrid climate dataset for the ARB. Eum and Gupta (2019) showed that REFRES hybrid climate dataset provides the best representation of historical climate in the ARB compared to other available datasets. The climate measurements are daily with spatial

resolution of $0.1° \times 0.1°$ or ~10 km within the ARB and available for the period of 1950–2019. The reader is referred to Eum and Gupta (2019) for more details.

The river flow measurements ($m^3 \, s^{-1}$) used in this study are obtained from the WSC database. The gauging stations selected in this study were chosen based on the availability of 55 years or more of continuous, year-round river flow measurements and situated at strategic locations within the ARB.

Herein, for all the multivariate regression and wavelet analyses, only the monthly accumulated precipitation, monthly averaged temperature, and river flow are considered. In other words, since the focus of this study is to investigate the correlation between river flow and climate in monthly scales, for each subregion, the daily river flows and daily temperatures in each month were averaged to obtain river flow and temperature time series with a sampling rate of 12 observations per year. Likewise, the sum of daily precipitations in each month was calculated to obtain the precipitation time series for each subregion. On the other hand, for the anomaly calculation, the annual accumulated precipitation, annual average temperature, and river flow are considered.

The annual LULC images are downloaded from the United States Geological Survey (USGS; https://earthexplorer.usgs.gov/). The images are obtained from *Terra* and *Aqua* Moderate Resolution Imaging Spectroradiometer (MODIS), namely MCD12Q1-V6, available only for the period 2001–19 at the time when this research was conducted. The MCD12Q1-V6 images are produced from supervised classifications of MODIS *Terra* and *Aqua* reflectance data that went through some additional postprocessing to improve the total of 11 LULC classes. The LULC images are yearly and have spatial resolution of 500 m.

c. Climate and flow anomalies procedure

Anomalies in yearly accumulated precipitation, yearly averaged temperature, and river flow were calculated by subtracting the baseline average (1961–90) from the yearly measurements. More precisely, the average of all grid values for each subregion for the climate was first calculated, then the yearly averaged temperature and yearly accumulated precipitation were calculated, and finally, the averages of yearly averaged temperatures and accumulated precipitation for period 1961–90 were subtracted from the yearly measurements. For the river flow, the measurements ($m^3 \, s^{-1}$) recorded at stations S1, S2, and S3 (the outlets of the three subregions) were used to calculate the anomalies with the same baseline period. Thirty-year-long baseline periods have been used in many studies for anomaly calculations (Eum et al. 2016; Lyra et al. 2016). The 30-yr period is a standard period recommended by the Intergovernmental Panel on Climate Change (IPCC) that can capture a range of climate variations, such as severe drought, floods, and cool and warm seasons. The World Meteorological Organization (WMO) standard baseline period 1961–90 suggested in Carter et al. (1994) is chosen herein. In this research, this baseline period is the oldest period when the river flow measurements for all the three

stations are available, and so one can study recent changes in climate and river flow with respect to the baseline.

d. Multivariate regression

Multivariate regression was performed on the river flow and climate measurements, where the temperature and precipitation were independent variables and river flow was the dependent variable. The formula used for regression was

$$\text{flow} = b_0 + b_1 \times P + b_2 \times T_{\text{avg}} + b_3 \times P \times T_{\text{avg}}, \quad (1)$$

where T_{avg} is monthly average temperature, and P is monthly accumulated precipitation. The coefficients b_0, b_1, b_2, and b_3 were estimated by the method of least squares (Draper and Smith 1981; Ghaderpour et al. 2021). These coefficients, along with the r value and p value were calculated for each regression model using the "regress" command in MATLAB; see Chatterjee and Hadi (1986) for more details. The measurements were chronologically classified and subdivided, where regression was performed on each subset separately. These subsets were monthly (e.g., only January between 1958 and 2020), all the months in the open warm season, cold season, and whole year. The open warm season included the months of May–October in station S1 and April–October in stations S2 and S3, while the cold season average included the rest of the year (Zaghloul et al. 2022).

e. LSCWA-3

Least squares cross-wavelet analysis (LSCWA) was proposed for estimating the coherency between wavelike components of two time series (Ghaderpour 2021a; Ghaderpour et al. 2018). The advantages of LSCWA over the traditional cross-wavelet transform and wavelet coherence (Torrence and Compo 1998) include finer time-frequency resolution, direct processing of time series with different sampling rates or missing values, and accounting for measurement errors.

Least squares triple cross-wavelet analysis (LSCWA-3) is like the LSCWA proposed herein for analyzing three time series together. In other words, the LSCWA-3 is a time–frequency technique developed for coherency analysis between the wavelike components of three time series. In the LSCWA-3, a common time vector is selected first, and then each time series is segmented according to a selected set of frequencies. The common time vector may be selected as the union of the three sets of times in the three time series. In this study, since all the time series are monthly (their sampling rate is 12 observations per year) with possibly some missing values, the common time vectors are also monthly (in the form of 1/12, 2/12, 3/12, ... years). Next, a spectrogram is estimated for each time series which has three dimensions, time, frequency, and normalized variance (Ghaderpour and Pagiatakis 2017). A Gaussian window function is chosen to produce an optimal time–frequency resolution spectrogram. The window expands over time as frequency increases and dilates as frequency decreases. As the window translates over time, harmonics and other constituents, such as trends, will be fitted to the segments within the window via the weighted least squares method. This
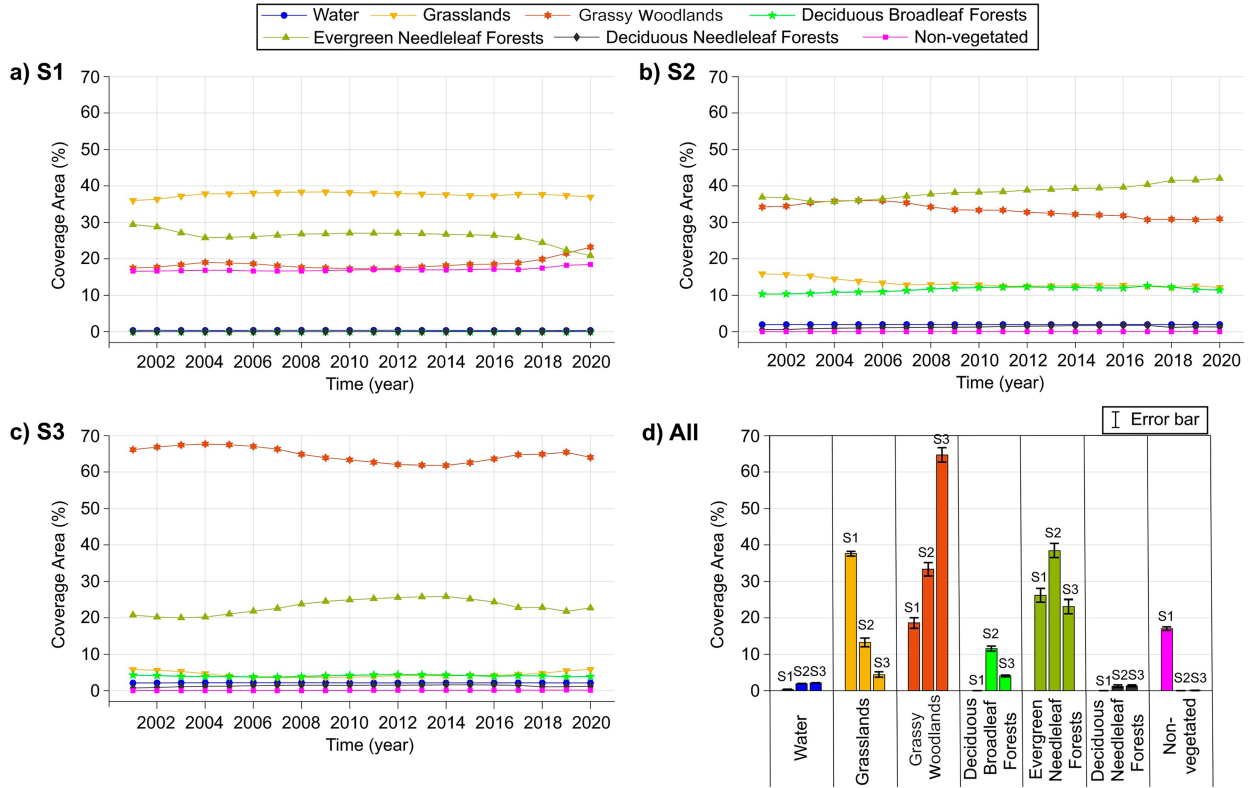
FIG. 2. The estimated annual time series of the LULC classes for each subregion of the ARB whose outlet is at (a) Hinton, (b) Athabasca, and (c) Fort McMurray, and (d) the bar chart showing the averages and standard deviations of the LULC classes, which are also listed in Table 1. The Sen's slopes and their p values for each LULC class are listed in Table 1.

process is done as the window translates over time and dilates over frequency to estimate a set of least squares spectral peaks, producing a spectrogram (Ghaderpour and Pagiatakis 2017). Since a common set of times and frequencies are selected for computing a spectrogram for each time series, the three spectrograms can then be elementwise multiplied by each other to produce a triple cross-spectrogram (LSCWS-3). Herein, three spectrograms are multiplied by each other, namely, the spectrograms of river flow, precipitation, and temperature time series.

Mathematically, to estimate one spectrogram for a given time series, the following cost function will be minimized for each segment of the time series.

$$\psi_k(t_i) = f_k(t_i) - c_0 a_0(t_i) - \cdots - c_q a_q(t_i) - c_{q+1}\cos(2\pi\omega_k t_i) - c_{q+2}\sin(2\pi\omega_k t_i), \tag{2}$$

where t_i is a time in the series segment, $f(t_i)$ is the measurement at t_i (e.g., river flow at t_i), and $a_0, \ldots, a_q$ are the constituents of known forms. Herein, $a_0(t_i) = 1$ (for all i) is selected for making the mean of the residual segment zero before estimating the spectrum. Also, since it is shown that the annual peaks of climate and river flow in this study are coherent, $a_1(t_i) = \cos(2\pi t_i)$ and $a_2(t_i) = \sin(2\pi t_i)$ are selected to calculate the residual cross-spectrogram for detecting other *hidden*

coherent peaks. Parameters $c_1, \ldots, c_q, c_{q+1}, c_{q+2}$ are unknowns and will be estimated by the weighted least squares method, where the weights are the Gaussian values, and ω_k is a cyclic frequency of interest. Since the Gaussian values are chosen, the measurements toward the center of each segment will have relatively higher weights than the measurements toward both sides of the segment. This way, the harmonics are adapted to Morlet wavelet in the least squares sense, generating an optimal time–frequency resolution spectrogram (Ghaderpour and Pagiatakis 2017). First, the residual segment is estimated by minimizing the cost function ψ_k without the harmonics at frequency ω_k. Thus, the residual is estimated as

$$r_k(t_i) = f_k(t_i) - \hat{c}_0 a_0(t_i) - \cdots - \hat{c}_q a_q(t_i), \tag{3}$$

where the hat symbol means estimated. Then all the unknown parameters c_j in Eq. (2) are estimated for each ω_k via the weighted least squares method (Ghaderpour and Pagiatakis 2017). After the estimation of the harmonic coefficients in Eq. (2), the following equation is derived:

$$h_k(t_i) = \hat{c}_{q+1}\cos(2\pi\omega_k t_i) + \hat{c}_{q+2}\sin(2\pi\omega_k t_i). \tag{4}$$

The least squares spectral peak at ω_k is defined as the weighted inner product of r_k and h_k divided by the weighted inner product of r_k and r_k or the weighted norm of r_k, where

TABLE 1. Mean and standard deviation of the number of pixels corresponding to different LULC classes in the subregions of the ARB. The other four LULC classes (broadleaf croplands and evergreen broadleaf forests, shrublands, and urban) were insignificant and are not listed here. The Sen's slope is in percent area per decade, and the boldface Sen's slopes are statistically significant at 95% confidence level (p value < 0.05).

	Hinton (S1)				Athabasca (S2)				Fort McMurray (S3)			
LULC class	Mean	SD	Slope	p value	Mean	SD	Slope	p value	Mean	SD	Slope	p value
Water	0.36	0.03	**−0.03**	0.04	1.97	0.01	0.00	0.31	2.17	0.02	−0.01	0.15
Grasslands	37.59	0.61	−0.22	0.46	13.26	1.13	**−1.37**	0.00	4.45	0.75	0.41	0.14
Grassy woodlands	18.59	1.45	**1.02**	0.04	33.30	1.77	**−2.94**	0.00	64.72	1.94	**−2.10**	0.02
Deciduous broadleaf forests	0.03	0.00	0.00	0.22	11.58	0.70	**1.09**	0.00	4.08	0.21	−0.01	0.97
Evergreen needleleaf forests	26.22	1.84	**−1.57**	0.00	38.44	1.89	**3.28**	0.00	23.11	1.96	**2.05**	0.02
Deciduous needleleaf forests	0.04	0.01	**0.01**	0.00	1.26	0.34	**0.66**	0.00	1.35	0.25	**0.21**	0.02
Nonvegetated lands	17.04	0.48	**0.44**	0.00	0.04	0.01	**0.01**	0.00	0.10	0.03	**0.04**	0.00

the weights are the same Gaussian values as mentioned above. The weights can also be adjusted according to measurement errors; that is, the inverse of measurement variance may be multiplied by the Gaussian value assigned to each measurement within a segment (Ghaderpour 2021a). For example, the daily river flow and temperature measurements can be converted to monthly measurements by calculating their averages along with their variances (e.g., the mean and variance of 31 measurements for January, etc.).

The collection of all the spectral peaks estimated at each time and each frequency produces a spectrogram. The spectral peaks in the spectrogram have the property that their frequency resolution reduces at larger frequencies while their time resolution increases and vice versa (Ghaderpour and Pagiatakis 2017). Herein, the cross multiplication of three least squares wavelet spectrograms, denoted by LSCWS-3, presents localized time–frequency peaks in terms of percentage variance, where their higher values indicate the higher coherency between cyclic components of the three time series.

The variance of 100% corresponding to a pair of time and frequency indicates that the local cycles of the three time series in a small time–frequency neighborhood, centered at the given pair, are perfectly coherent (no noise). In practice, the percentage variance of 15% or higher for peaks in cross-spectrograms (double-cross) and 5% or higher for peaks in cross-spectrograms (triple-cross) are considered significant. In this work, for each time series, the residual spectrogram is obtained by simultaneously estimating and removing the annual cycle in each segment as described by Ghaderpour and Pagiatakis (2017). The process of estimating and removing the annual cycles is done for each time series independently, and then the residual spectrograms of the time series are cross-multiplied to obtain the residual triple cross-spectrogram (residual LSCWS-3). The statistical significance of peaks in the cross-spectrograms can be determined from the normality and statistical independence of measurements in different time series (Ghaderpour et al. 2018). In this research, the peaks whose variance are greater than 5% are also statistically significant at 99% confidence level.
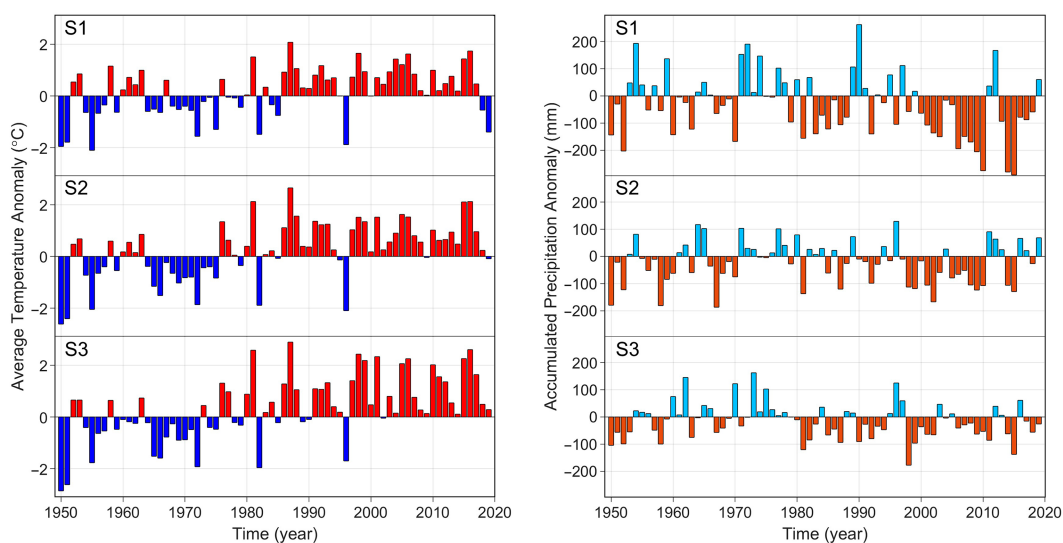

FIG. 3. The temperature and precipitation anomaly bar charts for the three subregions where the baseline period is 1961–90.
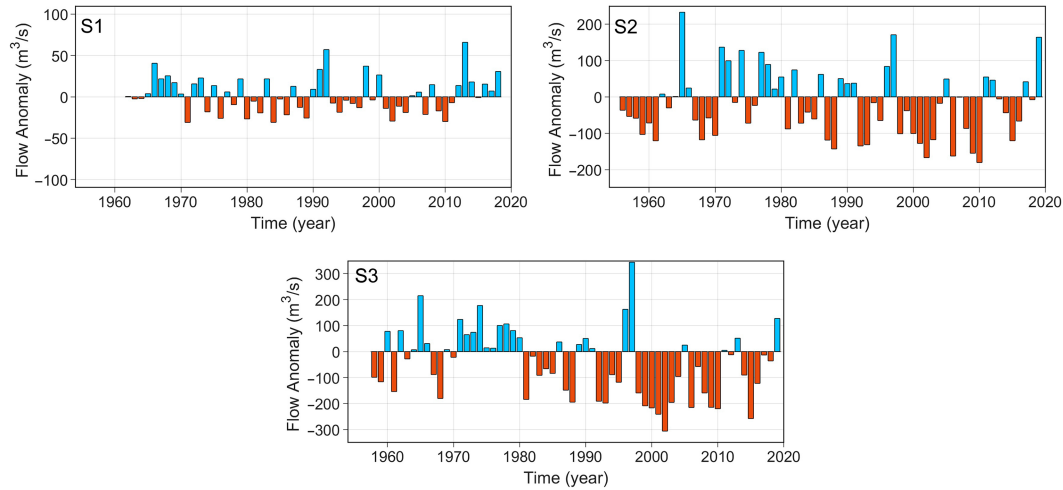
FIG. 4. The river flow anomaly bar charts for the three subregions where the baseline period is 1961–90.

To estimate phase delays between cycles of river flow and climate, the same procedure is followed as described by Ghaderpour et al. (2018) for each pair of time series (i.e., for river flow and precipitation time series and for river flow and temperature time series). Mathematically,

$$\sin(2\pi\omega_k t_i + \theta_k) = \sin(\theta_k)\cos(2\pi\omega_k t_i) + \cos(\theta_k)\sin(2\pi\omega_k t_i) \tag{5}$$

and Eq. (4) yield $\hat{c}_{q+1} = \sin(\theta_k)$ and $\hat{c}_{q+2} = \cos(\theta_k)$, and so θ_k for river flow and climate segments can be estimated

(Ghaderpour et al. 2018). For example, if $\hat{\theta}_{1k}$ and $\hat{\theta}_{2k}$ are the estimated phases for river flow and precipitation segments, then $\psi_k = \hat{\theta}_{1k} - \hat{\theta}_{2k}$ will be the estimated phase delay between the corresponding cycles of river flow and precipitation, shown by arrows in the cross-spectrograms. The phase arrows follow the trigonometric circle principle (e.g., Dastour et al. 2022). In addition, the phase can be converted from radians to days using the following relation: $t = 356.256/(2\pi) \times \psi_k/\omega_k$, where ω_k is in cycles per year.

In this research, the least squares cross-spectrum (LSCS) is also calculated by multiplying the spectra of the three time
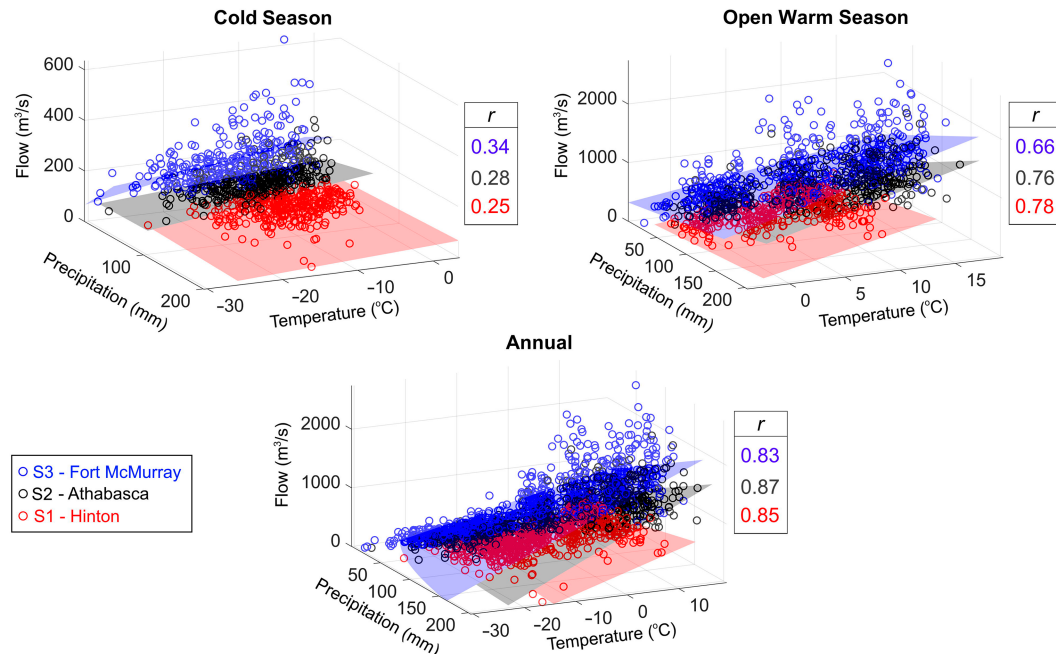

FIG. 5. Multivariate regression results for river flow, precipitation, and temperature. The *p* values for all the regressions are less than 0.0001. The estimated regression coefficients are listed in Table 3.
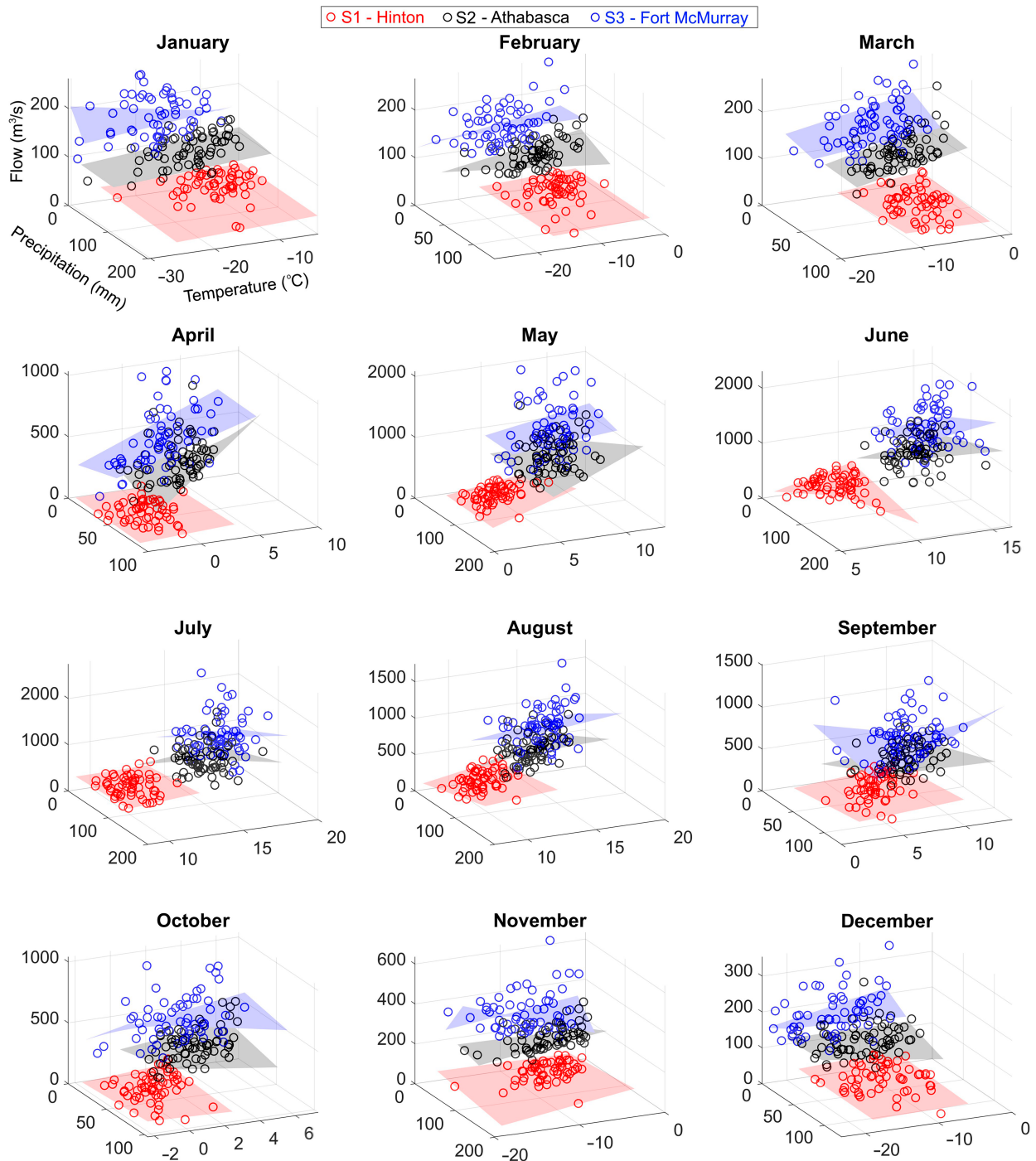
FIG. 6. The monthly multivariate regression analyses for temperature, precipitation, and river flow. The *r* and *p* values of these regressions are listed in Table 2, and their estimated coefficients are listed in Table 3.

series. There is no segmentation of the time series when LSCS is calculated; that is, the harmonics and trends are fitted to the entire time series only and the time series are decomposed into only the frequency domain not into the time–frequency domain. Ghaderpour et al. (2018) describe the LSCS for two time series, and herein the algorithm is naturally

extended for three time series to calculate triple cross-spectra (LSCS-3). In the present work, the antileakage least squares spectral analysis (ALLSSA) is also applied to the river flow and climate time series to simultaneously estimate their trend and harmonic components. The ALLSSA is a robust method of estimating the gradients in time series with seasonality (see

TABLE 2. The r and p values of the multivariate regression results shown in Fig. 6. The boldface r values are statistically significant at a 99% confidence level.

Month	S1		S2		S3	
	r	p value	r	p value	r	p value
Jan	0.27	0.256	0.25	0.264	0.10	0.898
Feb	0.34	0.082	0.22	0.391	0.19	0.537
Mar	0.36	0.061	0.41	0.011	0.33	0.088
Apr	0.42	0.017	0.32	0.081	0.38	0.035
May	**0.78**	0.000	0.21	0.430	0.15	0.730
Jun	**0.51**	0.001	**0.48**	0.001	0.32	0.099
Jul	0.30	0.168	**0.54**	0.000	0.30	0.139
Aug	**0.63**	0.000	**0.53**	0.000	0.39	0.024
Sep	**0.48**	0.003	**0.49**	0.001	**0.44**	0.005
Oct	0.27	0.258	0.15	0.697	0.21	0.436
Nov	0.30	0.180	0.11	0.858	0.21	0.445
Dec	0.28	0.210	0.14	0.759	0.20	0.497

Ghaderpour et al. 2021). The MATLAB and python software packages used for estimating season-trend components, spectra, and spectrograms are publicly available at https://geodesy.noaa.gov/gps-toolbox/JUST.htm (Ghaderpour 2021b).

3. Results

The percentage coverage of each LULC class was calculated for each subregion and each year from 2001 to 2020, illustrated in Fig. 2. Table 1 shows the mean and standard deviations of the LULC classes. Slopes and their p values for time series shown in Fig. 2 are estimated via the nonparametric Mann–Kendall (MK) and Sen's slope estimator, and the results are listed in Table 1; see Zaghloul et al. (2022) for the mathematical formula of MK and Sen's slope. The first subregion (S1), the mountainous region, had the highest nonvegetated lands (17% on average). Figure 2b and Table 1 show a slight increase in evergreen needleleaf forests (3.28% per decade) and a slight decrease in grassy

woodlands (−2.94% per decade). From Fig. 2, grasslands, grassy woodlands, and evergreen needleleaf forests had the highest percentage coverage and standard deviation for all the three subregions; however, the standard deviations were not significant. From Table 1, evergreen needleleaf forests in S1 have been decreasing with a rate of −1.57% per decade while nonvegetated lands have been increasing by 0.44% per decade since 2001 at 99% confidence level. The significant amount of nonvegetated lands and grasslands in the S1 subregion contributed to warming of this subregion and gradual glacier melts, which resulted in a gradual increase in river flow at S1 (Zaghloul et al. 2022).

The annual climate and river flow anomaly charts are displayed in Figs. 3 and 4, respectively. All three subregions show a significant temperature increase and precipitation decrease with respect to the baseline since 1991. Each subregion is shown by its representative hydrometric station (i.e., S1, S2, S3).

The multivariate regression results for the three subregions are illustrated in Fig. 5. The open warm season for all the three subregions shows a significantly higher correlation than the cold season. The highest correlation of 0.87 was for the entire monthly derived measurements (annual) corresponding to the subregion between Hinton and Athabasca (i.e., between S1 and S2). Note that the data points shown in the bottom panel of Fig. 5 (annual) are the total data points for the open warm season and cold season shown on the top two panels. In other words, for the annual panel, the multivariate regression was done on the entire monthly measurements. Note that each data point shown in Figs. 5 and 6 represents a triple value (temperature, precipitation, flow) for a particular month. Note that the triples were considered wherever river flow was available; that is, no gap-filling method was applied.

Figure 6 shows the multivariate regression results for each month separately, and Table 2 lists the correlation r and p values for regression results of each month. Table 3

TABLE 3. The estimated coefficients of the multivariate regression using Eq. (1). Note that b_0, b_1, b_2, and b_3 are the coefficients of intercept, precipitation, temperature, and precipitation multiplied by temperature, respectively.

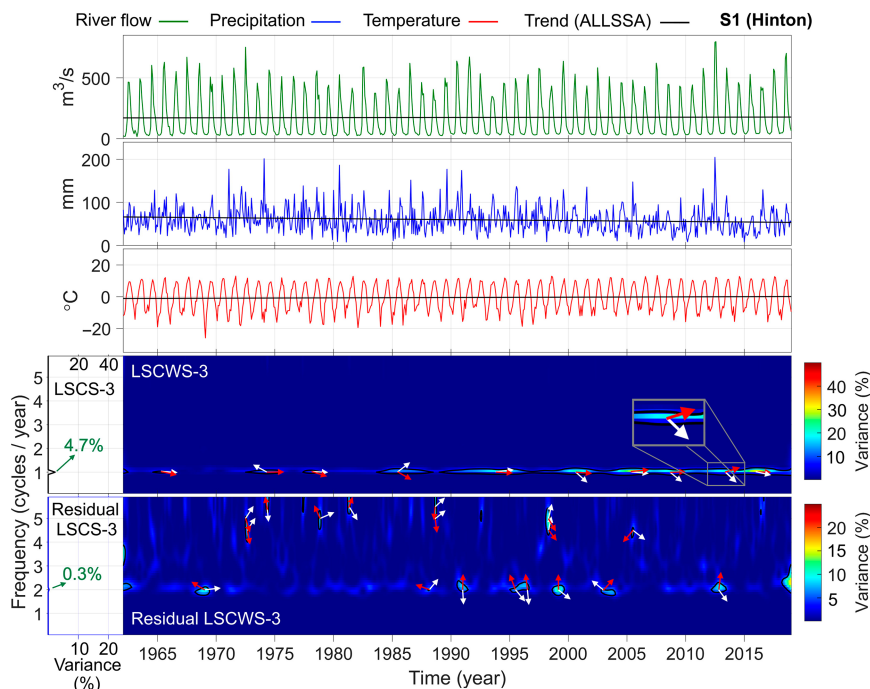| Date	S1				S2				S3			
	b_0	b_1	b_2	b_3	b_0	b_1	b_2	b_3	b_0	b_1	b_2	b_3
Jan	41.0	0.0	0.3	0.0	116.6	−0.1	1.2	0.0	126.9	1.6	−2.9	0.1
Feb	38.3	0.0	0.6	0.0	113.5	−0.7	2.3	−0.1	178.5	−0.1	2.2	−0.1
Mar	44.7	−0.1	2.0	0.0	123.8	−0.2	4.0	0.0	204.9	−1.1	3.2	0.0
Apr	44.9	0.1	−0.1	0.1	294.6	−0.6	−14.4	1.4	406.7	1.4	37.7	−0.2
May	49.1	−0.8	21.5	0.4	606.7	−3.2	−4.0	0.6	729.6	1.2	37.8	−0.2
Jun	−363.9	10.1	100.7	−1.2	80.2	7.7	41.9	−0.3	759.5	2.3	18.7	0.1
Jul	409.4	−0.8	0.1	0.2	−216.3	13.4	46.5	−0.6	1073.8	8.4	−11.1	−0.2
Aug	−122.6	2.6	35.1	−0.1	−464.7	8.7	58.3	−0.3	341.8	4.2	22.3	0.0
Sep	72.3	1.2	12.0	0.0	199.4	4.2	10.0	−0.1	968.3	−5.0	−48.4	1.0
Oct	111.7	0.1	13.5	−0.2	233.3	1.8	19.9	−0.5	379.2	5.0	28.9	−0.9
Nov	52.0	0.3	−1.0	0.0	156.1	1.1	−1.5	0.1	362.1	−3.5	7.8	−0.4
Dec	56.2	−0.1	1.0	0.0	123.4	−0.9	0.1	0.0	274.9	−2.3	5.0	−0.1
Cold season	43.1	0.1	0.3	0.0	126.5	0.6	2.2	0.0	231.9	1.3	5.6	−0.1
Warm season	51.3	1.0	22.7	0.1	195.9	2.8	15.0	0.2	422.1	2.5	26.8	0.2
Annual	90.5	1.5	10.7	0.1	181.8	3.7	11.5	0.2	401.4	4.5	19.2	0.1

FIG. 7. The triple cross-spectra and triple cross-spectrograms for river flow, precipitation, and temperature time series in the S1 subregion (Hinton). The spectral peaks whose variance is greater than 5% are significant at the 99% confidence level. In the cross-spectrograms, the significant peaks are shown inside the closed curves in black. The white arrows show phase delays between river flow and precipitation cycles while the red arrows show phase delays between river flow and temperature cycles. The arrows pointing to the right and left mean in phase and out of phase, respectively. The arrows pointing up and down show river flow cycles lead and lag, respectively (also see Fig. 10). The linear trend for each time series is shown by the straight black lines whose intercepts and slopes and their errors are shown in Table 4. Note that ALLSSA has estimated these trends simultaneously with harmonics at 99% confidence level.

shows the estimated multivariate regression coefficients that are used to plot the regression surfaces in Figs. 5 and 6. One can observe that for the mountainous subregion with outlet S1, January and May show the lowest (0.27) and highest (0.78) correlations, respectively. Moreover, river flow at S1 showed no correlation with precipitation during January and February as seen in Table 3. On the other hand, precipitation and temperature were positively correlated with river flow in June for S1. For the subregion between S1 and S2, the lowest and highest correlations were for November (0.11) and July (0.54), respectively. Furthermore, the subregion between S2 and S3 showed the lowest (0.10) and highest (0.44) correlation for January and September, respectively. Generally, all the subregions showed relatively higher positive correlations with precipitation and temperature during the open warm season than during the cold season (see Fig. 5 and Table 3). Note that the r values in Fig. 5 and Table 2 are calculated for the entire mathematical model given by Eq. (1), not to be confused with the coefficients in Table 3.

Other parameters, such as evapotranspiration, solar radiation, air pressure, and wind speed could also be modeled in multivariate regression; however, their contributions are either

insignificant or highly correlated with temperature, precipitation, and land cover that are already utilized in this study. In fact, in various studies, temperature and precipitation were found to be the major climatic factors affecting river flow as determined by statistical methods and tools, such as principal component analysis and SWAT (Lei et al. 2021; Zaghloul et al. 2022; Si et al. 2023).

To further investigate the temporal relationships between river flow and climate, the LSCSA-3 is applied to the time series of each subregion (i.e., the time series whose values are illustrated in the bottom panel of Fig. 5), and the results are shown in Figs. 7–9. Note that the time series are monthly (i.e., 12 observations per year). The daily river flows and temperatures for each month were averaged to obtain monthly river flow and temperature time series. Moreover, the sum of daily precipitation for each month was calculated to obtain the precipitation time series. The residual LSCWS-3 is obtained after simultaneously estimating and removing the annual cycle from river flow, precipitation, and temperature time series. The annual cycles of the climate and river flow measurements are coherent for all the three subregions; however, the lowest annual coherency of 4.7% is estimated for S1, while the annual coherencies of 30.5% and 33.7% are estimated for S2
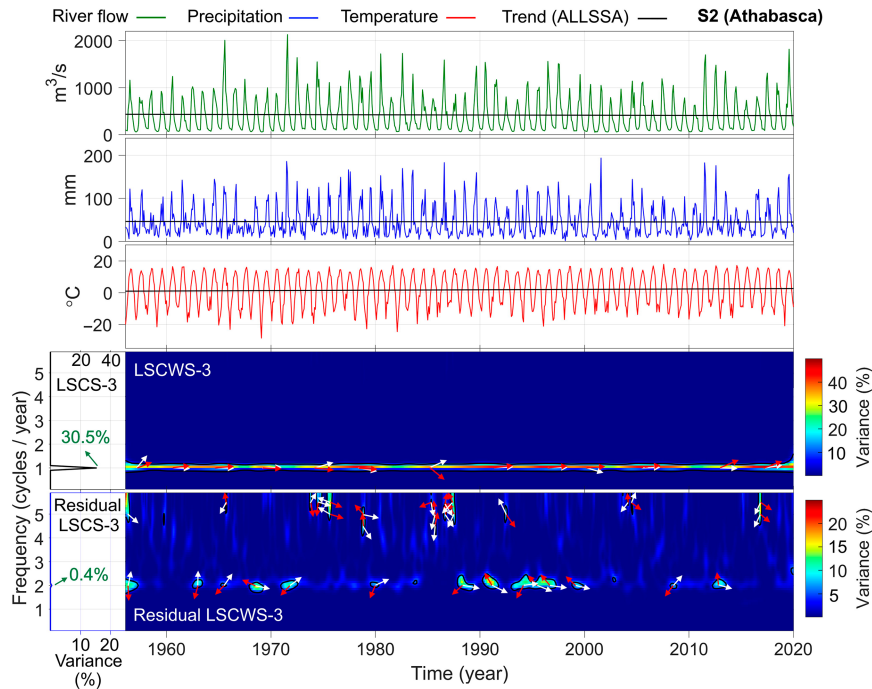
FIG. 8. As in Fig. 7, but for the S2 subregion (Athabasca).

and S3, respectively. The LSCWS-3 in Fig. 7 shows that the coherency between the annual cycles of the climate and river flow has increased since 1991, particularly in 2005 and 2015, because of the more significant annual cycles in the precipitation time series since 1991. Next, by simultaneously

estimating and removing the annual cycles in the climate and river flow time series segments, the residual LSCWS-3 is obtained. Interestingly, the results show coherent semiannual cycles (2 cycles per year or about 183 days) most of the time, while higher seasonal cycles occasionally show significant
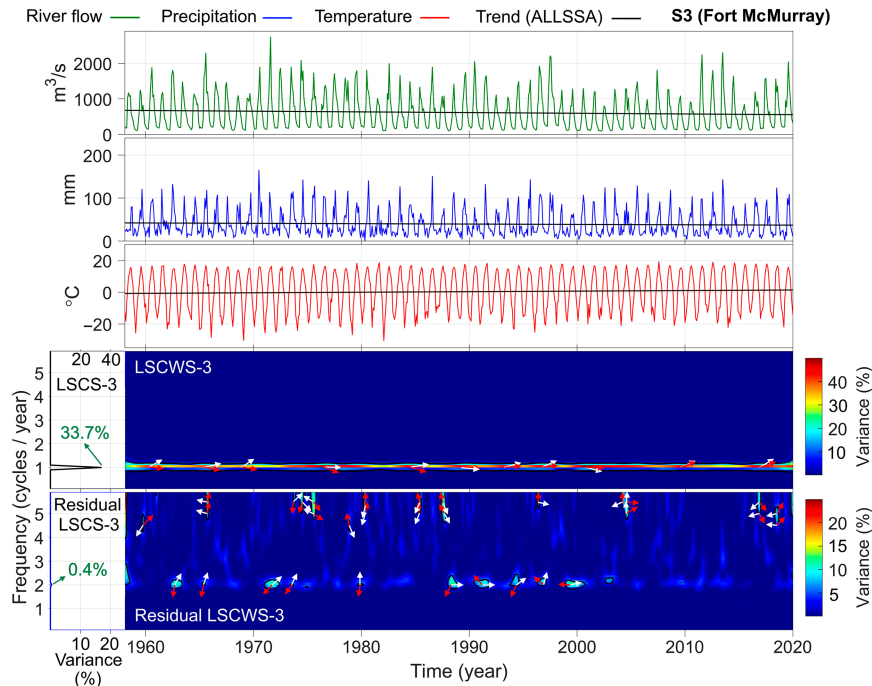

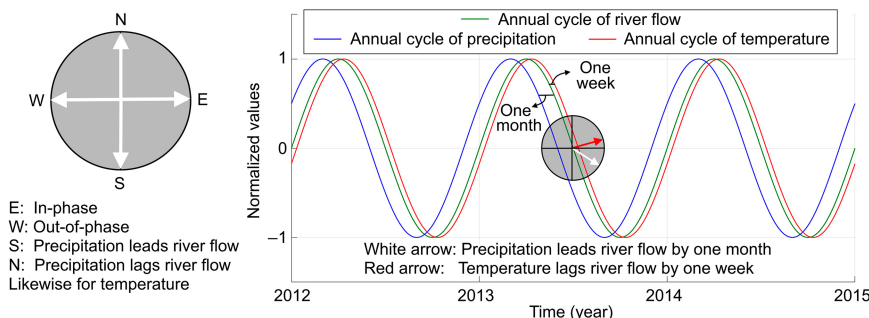FIG. 9. As in Fig. 7, but for the S3 subregion (Fort McMurray).

FIG. 10. An example of phase delay analysis for S1 (Hinton) from 2012 to 2015, shown in Fig. 7. The estimated annual cycles are normalized to aid phase delay visualization.

coherency over time (see the cross-spectrograms illustrated in the bottom panels of Figs. 7–9). For example, in Fig. 8, a relatively higher coherency can be observed for the semiannual cycles between 1990 and 2000 with more than 15% in 1990 (see the peaks inside the closed black curves). Note that as recommended by Torrence and Compo (1998) and Ghaderpour (2021a,b), six cycles of harmonics are fitted to each segment for each frequency to generate the spectrograms. This means at 1 cycle per year, 6 years of monthly measurements are used whereas at 2 cycles per year, 3 years of monthly measurements are used for each segment, and so on. Since the Gaussian weights are used (i.e., Morlet wavelets in the least squares sense), the measurements within the middle years of each segment get relatively higher weights. For example, higher weights are assigned to measurements in year 2001 for a segment that starts from 2000 and ends at the end of 2002 at 2 cycles per year, etc.

Figures 7–9 also show the phase delay results between the cycles of river flow and precipitation (white arrows) and river flow and temperature (red arrows). To better understand how to interpret the arrows, the estimated annual cycles between river flow and climate for S1, centered in 2013, are displayed in Fig. 10, showing that the precipitation leads river flow by one month while the temperature lags river flow by one week. The magnified section in LSCWS-3 in Fig. 7 demonstrates the corresponding triple spectra for the segments of the three time series whose normalized annual cycles are illustrated in Fig. 10. Note that for brevity and visualization purposes, the phase delay results (arrows) are only displayed for the most significant triple spectral peaks whose values are largest within a small neighborhood.

The ALLSSA season-trend estimates are listed in Table 4, showing that the river flows at S2 and S3 were gradually decreasing at a significant rate while the river flow at S1 was increasing insignificantly over the past six decades. The precipitation had a deceasing trend while the temperature had an increasing trend over the past six decades for all the three subregions. Table 4 also shows the amplitudes (along with their standard errors) of the seasonal cycles estimated simultaneously with the trend.

Table 5 shows the percentage coherency between river flow and precipitation and between river flow and temperature time series using LSCSA. From this table, the annual cycle of river flow is more coherent with the one in temperature than the one in precipitation for all the three subregions.

4. Discussion

Table 6 shows the river slope (Cohen et al. 2018) and most dominant soil groups and land cover types of the three subregions. For each subregion, the river slope was computed as the elevation difference between the hydrometric stations (from inlet to outlet) divided by the river length between the stations, that is, from near Jasper to Hinton (S1), from Hinton to Athabasca (S2), and from Athabasca to Fort McMurray (S3). The river slope is expressed by percentage in Table 6. For example, 0.13% for S1 means an elevation change of 1.3 m per 1-km distance along the river. To estimate the river slopes, the elevations of Athabasca River near Jasper (∼1059 m), at Hinton (∼954 m), at Athabasca (∼516 m), and below Fort McMurray (∼237 m) were used (Zaghloul et al. 2022). The river length for each subregion was estimated using Google Maps, which agrees with the results illustrated in Fig. 7 in Hwang et al. (2023).

As demonstrated in Fig. 2 and Table 6, the first subregion (before S1) has the highest nonvegetated land (17%) with about 38% grassland coverage and a relatively smaller area and steeper slope compared to the rest of the ARB. The correlation of 0.78 in May could then be explained as a more straightforward relationship between the warming (snowpack melting), precipitation, and runoff, which agrees with the results by Zhang et al. (2001), Burn and Elnur (2002), and Zaghloul et al. (2022). The subregion between S1 and S2 (or simply S2) is mostly covered by grassy woodlands (33%) and evergreen needleleaf forests (38%). Furthermore, the soil group of this subregion (gray luvisols and dark gray chernozemics) could potentially cause a delay between climate and runoff and may explain the low correlation of 0.54 in July (see Tables 2 and 6). The subregion between S2 and S3 (or simply S3) has about 65% grassy woodlands and 23% evergreen needle forests, deviating about 2% since 2001, with a relatively wider area and flatter terrain. Considering its soil group (gray luvisols and organics), agricultural and other human activities, the relatively lower correlation between climate and river flow could be explained (with a maximum of 0.44 in September) which agrees with the results of other similar studies (e.g.,

TABLE 4. The ALLSSA season-trend estimates at 99% confidence level for the time series shown in Figs. 7–9. The estimated intercepts for S1, S2, and S3 are in years 1962, 1956, and 1958, respectively. The boldface slopes are significant.

Type of time series	Subregion	Intercept (unit)	Slope (unit yr^{-1})	Amplitude				
				1 cycle per year	2 cycles per year	3 cycles per year	4 cycles per year	5 cycles per year
River flow	S1	170.5 ± 3.9 m^3 s^{-1}	0.119 ± 0.121 m^3 s^{-1} yr^{-1}	208.8 ± 2.8 m^3 s^{-1}	96.9 ± 2.8 m^3 s^{-1}	43.7 ± 2.8 m^3 s^{-1}	23.0 ± 2.8 m^3 s^{-1}	14.0 ± 2.8 m^3 s^{-1}
	S2	432.6 ± 13.1 m^3 s^{-1}	−0.450 ± 0.56 m^3 s^{-1} yr^{-1}	434.6 ± 9.3 m^3 s^{-1}	147.2 ± 9.3 m^3 s^{-1}	46.6 ± 9.3 m^3 s^{-1}	None	None
	S3	676.2 ± 18.1 m^3 s^{-1}	−1.947 ± 0.505 m^3 s^{-1} yr^{-1}	577.7 ± 12.7 m^3 s^{-1}	170.3 ± 12.7 m^3 s^{-1}	62.6 ± 12.8 m^3	None	None
Precip	S1	66.2 ± 2.1 mm	−0.222 ± 0.065 mm yr^{-1}	11.2 ± 1.5 mm	9.4 ± 1.5 mm	None	None	None
	S2	46.4 ± 1.6 mm	−0.021 ± 0.044 mm yr^{-1}	36.0 ± 1.1 mm	18.4 ± 1.1 mm	4.1 ± 1.1 mm	None	None
	S3	42.3 ± 1.3 mm	−0.082 ± 0.037 mm yr^{-1}	31.0 ± 0.9 mm	14.6 ± 0.9 mm	3.4 ± 0.9 mm	3.0 ± 0.9 mm	None
Temp	S1	−1.146° ± 0.2°C	0.021° ± 0.006°C yr^{-1}	11.2° ± 0.1°C	1.2° ± 0.1°C	None	None	None
	S2	0.935° ± 0.2°C	0.025° ± 0.006°C yr^{-1}	13.9° ± 0.1°C	1.1° ± 0.1°C	None	None	None
	S3	−0.668° ± 0.2°C	0.033° ± 0.006°C yr^{-1}	17.0° ± 0.2°C	1.4° ± 0.2°C	None	None	None

Wang et al. 2018). From the results shown in Tables 3 and 4 and Fig. 5, a gradual decrease in precipitation and increase in temperature are expected to decrease the river flow in the ARB during the open warm season, which agrees with the findings of Morales-Marín et al. (2019).

Figure 3 showed that the temperature and precipitation anomalies were mostly positive and negative with respect to the baseline during the past three decades, respectively. Figure 4 also showed that S1 mostly had positive river flow anomalies while S2 and S3 mostly had negative anomalies during the past three decades. This may be explained by gradual glaciers and snowpack melting in the mountainous region (before S1) due to temperature increase and albedo decrease in recent decades, contributing to runoff, while the other two subregions have more vegetation/forest coverage and are flatter as observed in Figs. 1 and 2 and Table 6 (Pradhananga and Pomeroy 2022; Zaghloul et al. 2022).

In the present study, the monthly derived measurements were separated, and then the multivariate regression was performed on the monthly measurements (e.g., July 1950, July 1951, …, July 2019). Furthermore, the annual, open warm season, and cold season regression were on the monthly measurements. The poor correlation between climate and river flow during the cold months could be explained by several reasons, such as ice formation and measurement errors, causing an irregular pattern in data clouds, as seen in Figs. 5 and 6 (Andrishak and Hicks 2011; Katopodis and Ghamry 2007). Furthermore, the air temperature variations are unlikely to influence the river flow if it remains below zero. From Table 2, the first subregion (before S1) shows a higher correlation than the other two subregions during cold months which may be explained by higher elevation, snowpacks and glacier melt, which contribute to river flow with some delays (May shows the highest correlation for S1). Ghaderpour et al. (2021) employed the LSCWA and showed that the annual and seasonal cycles of the precipitation generally led to the ones in the river flow, meaning there was a time delay (about a few weeks) between precipitation and river flow cycles. Neglecting such time delay in the regression could slightly decrease the Pearson correlation.

As illustrated in Figs. 7–9, the triple cross-spectra and cross-spectrograms of river flow, precipitation, and temperature showed significant coherency between their annual cycles, where the most annual coherency was observed for S2 and S3 subregions. For the mountainous subregion S1, the annual coherency was more significant since 1991. The main reason for the poor coherency before 1991 was an insignificant and discontinuous annual cycle in the precipitation time series that decreased the overall annual coherency, although both river flow and temperature time series had significant and continuous annual cycles. Recent land cover changes in the S1 subregion could have also played a role in annual cycles of precipitation since 1991. Another possible reason for higher annual coherency since 1991 as seen in Fig. 7 is gradual regional warming (see Table 4).

The white arrows in Fig. 7 show that the precipitation annual and semiannual cycles led the ones in river flow mainly since 1991 while the temperature cycles were almost in phase with the river flow cycles. This could be explained by the fact

TABLE 5. The percentage coherency between river flow and climate for the three ARB regions. All the values are statistically significant at 99% confidence level.

Subregion	River flow and precipitation annual coherency	River flow and temperature annual coherency	River flow and precipitation semiannual coherency	River flow and temperature semiannual coherency
S1	5.1%	64.8%	3.0%	5.8%
S2	33.4%	62.1%	6.1%	1.8%
S3	36.0%	64.5%	4.7%	1.8%

that in mountainous regions, the precipitation is usually in the form of snow, causing some delay in contributing to runoff during the snow melting process. Furthermore, the forest cover was significantly decreasing while the nonvegetated lands were increasing in the recent decades in S1 (see Table 1), which have reduced the physical obstructions to surface flow. On the other hand, Table 1 showed that forests were significantly increasing in recent decades in the relatively flatter subregions S2 and S3. This together with gradual warming, evapotranspiration, and anthropogenic activities (Lima and Wrona 2019) resulted in different phase delay patterns as illustrated by white and red arrows in Figs. 8 and 9. Furthermore, Autio et al. (2020) and Hwang et al. (2023) showed that spatial distribution of groundwater and surface water exchange can be highly impacted by peat soil characteristics, the main soils of subregion S3. As shown in Table 5, the precipitation cycles were much more coherent with river flow cycles in S2 and S3 than in S1, justifying why there is higher annual and semiannual coherency in triple cross-spectra and cross-spectrograms shown in Figs. 8 and 9. Note that the white arrows that are pointing toward north in the triple cross-spectrograms indicate that precipitation cycles lag river flow cycles, which may be explained by excessive evaporation and infiltration capacity of soil, plant root water absorption, and water withdrawals (Lima and Wrona 2019; Zaghloul et al. 2022; Hwang et al. 2023).

The hybrid precipitation measurements utilized in this research carried the information of snow and rain together, and so it was not possible to conduct more detailed analysis of rainfall versus snowfall. Exploring other potential meteorological datasets for this purpose is subject to future work. Since enough harmonic cycles were fitted to time series segments, the significant semiannual coherent peaks in

RLSCWS-3 in Figs. 8 and 9 likely have physical meanings (i.e., changing climate and their direct impact on river flow). For example, Fig. 9c in Ghaderpour et al. (2021) shows that the spectrogram of river flow at Athabasca (S2) has significant semiannual peaks between 1990 and 2000, and Fig. 8 in the present study shows that the climate time series (in particular, precipitation) had significant semiannual cycles between 1990 and 2000. It would be interesting to investigate the land cover changes between 1990 and 2000 to justify this coherency, unfortunately the MODIS images utilized here were available only after 2000.

Two of the main factors for gradual river flow decrease in ARB were gradual warming and declining precipitation as shown in Table 4 and Fig. 4. In addition, anthropogenic activities have also had an impact on river flow decrease, particularly in subregions S2 and S3, which experienced rapid development of urban, agriculture, and industry during the past few decades (e.g., pulp and paper mills and agriculture in S2 and oil sand mining in S3 and the lower ARB). Water withdrawals for municipal and industrial use have been significantly increased in recent decades (Lima and Wrona 2019). From Table 4 and Fig. 3, the precipitation in S1 has been decreasing at a faster rate (-0.22 mm yr^{-1}), which could likely be due to the recent land cover change in S1; that is, forests have been replaced by nonvegetated lands due to wildfire and/or deforestation during the past few decades (see Table 1 herein; Mahmood et al. 2010; Zaghloul et al. 2022).

Continuous monitoring of river flow is necessary for proper water management and performing more sustainable policies. However, these tasks are very challenging, particularly for cold climate regions like the ARB (Belvederesi et al. 2020b, 2022). Through a flow simulation via a hydrologic model based on the recent Coupled Model Intercomparison Project

TABLE 6. River slope and most dominant soil groups and land cover types of the ARB subregions. The upward and downward arrows indicate that the specific land cover has been increasing and decreasing since 2001, respectively (see Table 1).

Subregion	River slope (%)	Soil group	Dominant land cover type (%)
S1	0.13	Brunisols and gray luvisols	Grasslands 37.6 ↓ Grassy woodlands 18.6 ↑ Evergreen needleleaf forests 26.2 ↓ Nonvegetated land 17.0 ↑
S2	0.09	Gray luvisols and dark gray chernozemics	Grasslands 13.3 ↓ Grassy woodlands 33.3 ↓ Deciduous broadleaf forests 11.6 ↑ Evergreen needleleaf forests 38.4 ↑
S3	0.07	Gray luvisols and organics	Grassy woodlands 64.7 ↓ Evergreen needleleaf forests 23.1 ↑

(CMIP5), Dibike et al. (2019) predicted the river flow of the Athabasca River. They predicted an increase in river flow during the winter and spring but with a decline in the summer and early fall and with an overall increase, particularly at low-frequency peaks. However, their forecasting results were highly dependent on the climate model and streamflow measurements used for simulation. There are only a few stations along the Athabasca River that provide long-term historical measurements. Many of the gauging stations in the ARB only provide seasonal measurements and do not have a long history. In this research, the poor correlations between river flow and climate during the cold months (Table 2) are an indicator of the forecasting challenge. Since the precipitation shows irregular annual and seasonal patterns, especially in the mountainous subregion, its direct use for river flow forecasting can be a very difficult task. The interannual river flow variation can be estimated using several decades of measurements that can be used for long-term forecasting. For example, Chen and Grasby (2014) showed that the long-term trend in Athabasca River flow had a significant relationship with the Pacific decadal oscillation. In other words, the overall decreasing trend in Athabasca River flow since 1960, reported in many publications, could be the down limb part of a long periodic cycle (over a century). Finally, the LSCWA-3 provided another insight into how climate and river flow are dependent over time and frequency; that is, the triple cross-spectrograms showed that the coherency between climate and flow cycles changed over time, which may also be useful for forecasting applications (Ghaderpour et al. 2021).

5. Conclusions

In this work, a robust triple cross-wavelet analysis was proposed based on the least squares principle and was applied to monthly climate and river flow time series in the ARB to investigate their possible relationships in the time–frequency domain. This work is summarized as follows.

Materials: 1) Monthly resampled REFRES hybrid climate data provided by the government of Alberta since 1950 at 10-km spatial resolution, 2) monthly resampled river flow time series by WSC for three hydrometric stations S1, S2, and S3 since 1962, 1956, and 1958, respectively, and 3) annual MODIS land cover imagery since 2001 at 500-m resolution.

Methods: A multivariate regression analysis and new triple cross-spectral and cross-wavelet analyses were applied to river flow, precipitation, and temperature time series for three subregions of the ARB, labeled as S1, S2, and S3. Long-term trends in the climate and river flow for each subregion were also estimated by a robust season-trend fit model, namely ALLSSA. In addition, annual climate and river flow anomalies were also calculated.

Hydrologic findings: It was shown that the mountainous subregion of the ARB (Hinton: S1) had a higher correlation between climate and river flow than the other two subregions, particularly in May (0.78). The lowest correlations were found during the cold months. The correlations between climate and river flow were found to be significantly dependent on various factors, such as specific soil groups, topography, and land cover characteristics. The triple cross-spectrograms (LSCWS-3)

showed that the annual cycles of the river flow, precipitation, and temperature were significantly coherent, where the most and the least stable annual coherencies were found for S3 (33.7%) and S1 (4.7%) subregions. The semiannual and other intra-annual cycles of the river flow and climate time series were also coherent in certain periods. The annual and semiannual cycles of the precipitation generally led the ones in river flow mainly in S1 followed by S2 since 1991.

Advantages and limitations: Multivariate regression, LSCSA-3, and LSCWA-3 provided useful information. The LSCWA-3 estimated the coherency in the time–frequency domain, which provided more details as compared to the LSCSA-3 that is only in the frequency domain. Unlike traditional multivariate regression, LSCWA-3 showed how the climate and river flow cycles were coherent over time and how much they led/lagged from each other. Since LSCSA-3 and LSCWA-3 are based on the least squares principle, they can handle the time series with missing values and/or different sampling rates without any need for time alignment. The limitations of this research include a lack of long-term river flow measurements, a limited number of gauging stations, and a short period for LULC images (20 years) to create a more sophisticated spatiotemporal network for a better understanding of such relationships. The correlation and coherency between river flow and climate were shown at monthly scales to establish comparisons between multivariate regressions and triple-cross spectra and spectrograms. However, similar analyses can be performed on daily time series to investigate changes at higher-frequency cycles of climate and river flow. Unfortunately, there was no further information about industrial and agricultural water withdrawals across the ARB to investigate other possible causes of trend change in river flow more rigorously.

It is hoped that the methods and results presented here can further help scientists and responsible authorities to make proper decisions for water management. Continuous ground and remote sensing data acquisitions could potentially help scientists to better understand the hydrological characteristics of the ARB along with their triggering factors.

is available at Alberta Environment and Parks; contact the corresponding author.

River flow Measurements: Water Survey of Canada (https://wateroffice.ec.gc.ca/search/historical_e.html). Accessed 29 November 2021.

REFERENCES

Afrin, S., A. Gupta, B. Farjad, M. R. Ahmed, G. Achari, and Q. Hassan, 2019: Development of land-use/land-cover maps using Landsat-8 and MODIS data, and their integration for hydro-ecological applications. *Sensors*, **19**, 4891, https://doi.org/10.3390/s19224891.

Andrishak, R., and F. Hicks, 2011: Ice effects on flow distributions within the Athabasca Delta, Canada. *River Res. Appl.*, **27**, 1149–1158, https://doi.org/10.1002/rra.1414.

Autio, A., P. Ala-Aho, A.-K. Ronkanen, P. M. Rossi, and B. Kløve, 2020: Implications of peat soil conceptualization for groundwater exfiltration in numerical modeling: A study on a hypothetical peatland hillslope. *Water Resour. Res.*, **56**, e2019WR026203, https://doi.org/10.1029/2019WR026203.

Bawden, A. J., H. C. Linton, D. H. Burn, and T. D. Prowse, 2014: A spatiotemporal analysis of hydrological trends and variability in the Athabasca River region, Canada. *J. Hydrol.*, **509**, 333–342, https://doi.org/10.1016/j.jhydrol.2013.11.051.

Belvederesi, C., J. A. Dominic, Q. K. Hassan, A. Gupta, and G. Achari, 2020a: Predicting river flow using an AI-based sequential adaptive neuro-fuzzy inference system. *Water*, **12**, 1622, https://doi.org/10.3390/w12061622.

——, ——, ——, ——, and ——, 2020b: Short-term river flow forecasting framework and its application in cold climatic regions. *Water*, **12**, 3049, https://doi.org/10.3390/w12113049.

——, M. S. Zaghloul, G. Achari, A. Gupta, and Q. K. Hassan, 2022: Modelling river flow in cold and ungauged regions: A review of the purposes, methods, and challenges. *Environ. Rev.*, **30**, 159–173, https://doi.org/10.1139/er-2021-0043.

Burn, D. H., and M. A. H. Elnur, 2002: Detection of hydrologic trends and variability. *J. Hydrol.*, **255**, 107–122, https://doi.org/10.1016/S0022-1694(01)00514-5.

——, J. M. Abdul Aziz, and A. Pietroniro, 2004a: A comparison of trends in hydrological variables for two watersheds in the Mackenzie River basin. *Can. Water Resour. J.*, **29**, 283–298, https://doi.org/10.4296/cwrj283.

——, J. M. Cunderlik, and A. Pietroniro, 2004b: Hydrological trends and variability in the Liard River basin/Tendances hydrologiques et variabilité dans le basin de la rivière Liard. *Hydrol. Sci. J.*, **49**, 53–67, https://doi.org/10.1623/hysj.49.1.53.53994.

Carter, T. R., M. L. Parry, H. Harasawa, and S. Nishioka, 1994: IPCC technical guidelines for assessing climate change impacts and adaptations. IPCC Special Rep. CGER-I015-'94, 72 pp., https://www.ipcc.ch/site/assets/uploads/2018/03/ipcc-technical-guidelines-1994n-1.pdf.

Chatterjee, S., and A. S. Hadi, 1986: Influential observations, high leverage points, and outliers in linear regression. *Stat. Sci.*, **1**, 379–393, https://doi.org/10.1214/ss/1177013622.

Chen, Z., and S. E. Grasby, 2014: Reconstructing river discharge trends from climate variables and prediction of future trends. *J. Hydrol.*, **511**, 267–278, https://doi.org/10.1016/j.jhydrol.2014.01.049.

Cohen, S., T. Wan, M. Tazmul Islam, and J. P. M. Syvitski, 2018: Global river slope: A new geospatial dataset and global-scale analysis. *J. Hydrol.*, **563**, 1057–1067, https://doi.org/10.1016/j.jhydrol.2018.06.066.

Dastour, H., E. Ghaderpour, M. S. Zaghloul, B. Farjad, A. Gupta, H. Eum, G. Achari, and Q. K. Hassan, 2022: Wavelet-based spatiotemporal analyses of climate and vegetation for the Athabasca River Basin in Canada. *Int. J. Appl. Earth Obs. Geoinf.*, **114**, 103044, https://doi.org/10.1016/j.jag.2022.103044.

Dibike, Y., H.-I. Eum, and T. Prowse, 2018: Modelling the Athabasca watershed snow response to a changing climate. *J. Hydrol. Reg. Stud.*, **15**, 134–148, https://doi.org/10.1016/j.ejrh.2018.01.003.

——, ——, P. Coulibaly, and J. Hartmann, 2019: Projected changes in the frequency of peak flows along the Athabasca River: Sensitivity of results to statistical methods of analysis. *Climate*, **7**, 88, https://doi.org/10.3390/cli7070088.

Draper, N., and H. Smith, 1981: *Applied Regression Analysis*. 2nd ed. John Wiley and Sons, 709 pp.

Du, X., N. K. Shrestha, and J. Wang, 2019: Assessing climate change impacts on stream temperature in the Athabasca River Basin using SWAT equilibrium temperature model and its potential impacts on stream ecosystem. *Sci. Total Environ.*, **650**, 1872–1881, https://doi.org/10.1016/j.scitotenv.2018.09.344.

Eum, H.-I., and A. Gupta, 2019: Hybrid climate datasets from a climate data evaluation system and their impacts on hydrologic simulations for the Athabasca River Basin in Canada. *Hydrol. Earth Syst. Sci.*, **23**, 5151–5173, https://doi.org/10.5194/hess-23-5151-2019.

——, Y. Dibike, and T. Prowse, 2016: Comparative evaluation of the effects of climate and land-cover changes on hydrologic responses of the Muskeg River, Alberta, Canada. *J. Hydrol. Reg. Stud.*, **8**, 198–221, https://doi.org/10.1016/j.ejrh.2016.10.003.

——, ——, and ——, 2017: Climate-induced alteration of hydrologic indicators in the Athabasca River Basin, Alberta, Canada. *J. Hydrol.*, **544**, 327–342, https://doi.org/10.1016/j.jhydrol.2016.11.034.

Frelich, L. E., and P. B. Reich, 2010: Will environmental changes reinforce the impact of global warming on the prairie–forest border of central North America? *Front. Ecol. Environ.*, **8**, 371–378, https://doi.org/10.1890/080191.

Ghaderpour, E., 2021a: Least-squares wavelet and cross-wavelet analyses of VLBI baseline length and temperature time series: Fortaleza–Hartebeesthoek–Westford–Wettzell. *Publ. Astron. Soc. Pac.*, **133**, 014502, https://doi.org/10.1088/1538-3873/abcc4e.

——, 2021b: JUST: MATLAB and python software for change detection and time series analysis. *GPS Solutions*, **25**, 85, https://doi.org/10.1007/s10291-021-01118-x.

——, and S. D. Pagiatakis, 2017: Least-squares wavelet analysis of unequally spaced and non-stationary time series and its applications. *Math. Geosci.*, **49**, 819–844, https://doi.org/10.1007/s11004-017-9691-0.

——, E. S. Ince, and S. D. Pagiatakis, 2018: Least-squares cross-wavelet analysis and its applications in geophysical time series. *J. Geod.*, **92**, 1223–1236, https://doi.org/10.1007/s00190-018-1156-9.

——, T. Vujadinovic, and Q. K. Hassan, 2021: Application of the least-squares wavelet software in hydrology: Athabasca River Basin. *J. Hydrol. Reg. Stud.*, **36**, 100847, https://doi.org/10.1016/j.ejrh.2021.100847.

Gillanders, S. N., N. C. Coops, M. A. Wulder, and N. R. Goodwin, 2008: Application of Landsat satellite imagery to monitor land-cover changes at the Athabasca oil sands, Alberta,

Canada. *Can. Geogr.*, **52**, 466–485, https://doi.org/10.1111/j.1541-0064.2008.00225.x.

Hassan, Q. K., I. R. Ejiagha, M. R. Ahmed, A. Gupta, E. Rangelova, and A. Dewan, 2021: Remote sensing of local warming trend in Alberta, Canada during 2001–2020, and its relationship with large-scale atmospheric circulations. *Remote Sens.*, **13**, 3441, https://doi.org/10.3390/rs13173441.

Hebert, C. E., 2019: The river runs through it: The Athabasca River delivers mercury to aquatic birds breeding far downstream. *PLOS ONE*, **14**, e0206192, https://doi.org/10.1371/journal.pone.0206192.

Hwang, H.-T., Y.-J. Park, E. A. Sudicky, S. J. Berg, R. McLaughlin, and J. P. Jones, 2018: Understanding the water balance paradox in the Athabasca River Basin, Canada. *Hydrol. Processes*, **32**, 729–746, https://doi.org/10.1002/hyp.11449.

——, A. R. Erler, O. Khader, S. J. Berg, E. A. Sudicky, and J. P. Jones, 2023: Estimation of groundwater contributions to Athabasca River, Alberta, Canada. *J. Hydrol. Reg. Stud.*, **45**, 101301, https://doi.org/10.1016/j.ejrh.2022.101301.

Katopodis, C., and H. K. Ghamry, 2007: Hydrodynamic and physical assessment of ice-covered conditions for three reaches of the Athabasca River, Alberta, Canada. *Can. J. Civ. Eng.*, **34**, 717–730, https://doi.org/10.1139/l07-026.

Kerkhoven, E., T. Y. Gan, C.-C. Kuo, and Z. Islam, 2011: Unconditional uncertainties of historical and simulated river flows subjected to climate change. *Proc. Annual Conf. of the Canadian Society for Civil Engineering*, Ontario, Canada, Curran Associates, Inc., 3238–3248, https://doi.org/10.13140/2.1.3333.4083.

Khan, Z., and Coauthors, 2022: Climate–streamflow relationship and consequences of its instability in large rivers of Pakistan: An elasticity perspective. *Water*, **14**, 2033, https://doi.org/10.3390/w14132033.

Lavkulich, L. M., and J. M. Arocena, 2011: Luvisolic soils of Canada: Genesis, distribution, and classification. *Can. J. Soil Sci.*, **91**, 781–806, https://doi.org/10.4141/cjss2011-014.

Lei, Y., X. Jiang, W. Geng, J. Zhang, H. Zhao, and L. Ren, 2021: The variation characteristics and influencing factors of base flow of the Hexi Inland Rivers. *Atmosphere*, **12**, 356, https://doi.org/10.3390/atmos12030356.

Lima, A. C., and F. J. Wrona, 2019: Multiple threats and stressors to the Athabasca River Basin: What do we know so far? *Sci. Total Environ.*, **649**, 640–651, https://doi.org/10.1016/j.scitotenv.2018.08.285.

Lyra, A., P. Imbach, D. Rodriguez, S. C. Chou, S. Georgiou, and L. Garofolo, 2016: Projections of climate change impacts on Central America tropical rainforest. *Climatic Change*, **141**, 93–105, https://doi.org/10.1007/s10584-016-1790-2.

Mahmood, R., and Coauthors, 2010: Impacts of land use/land cover change on climate and future research priorities. *Bull. Amer. Meteor. Soc.*, **91**, 37–46, https://doi.org/10.1175/2009BAMS2769.1.

Monk, W. A., D. L. Peters, and D. J. Baird, 2012: Assessment of ecologically relevant hydrological variables influencing a cold-region river and its delta: The Athabasca River and the Peace-Athabasca Delta, northwestern Canada. *Hydrol. Processes*, **26**, 1827–1839, https://doi.org/10.1002/hyp.9307.

Morales-Marín, L. A., P. Rokaya, P. R. Sanyal, J. Sereda, and K. E. Lindenschmidt, 2019: Changes in streamflow and water temperature affect fish habitat in the Athabasca River Basin in the context of climate change. *Ecol. Modell.*, **407**, 108718, https://doi.org/10.1016/j.ecolmodel.2019.108718.

Pérez Ciria, T., and G. Chiogna, 2020: Intra-catchment comparison and classification of long-term streamflow variability in the Alps using wavelet analysis. *J. Hydrol.*, **587**, 124927, https://doi.org/10.1016/j.jhydrol.2020.124927.

Peters, D. L., D. Atkinson, W. A. Monk, D. E. Tenenbaum, and D. J. Baird, 2013: A multi-scale hydroclimatic analysis of runoff generation in the Athabasca River, western Canada. *Hydrol. Processes*, **27**, 1915–1934, https://doi.org/10.1002/hyp.9699.

——, D. Watt, K. Devito, W. A. Monk, R. R. Shrestha, and D. J. Baird, 2022: Changes in geographical runoff generation in regions affected by climate and resource development: A case study of the Athabasca River. *J. Hydrol. Reg. Stud.*, **39**, 100981, https://doi.org/10.1016/j.ejrh.2021.100981.

Pradhananga, D., and J. W. Pomeroy, 2022: Diagnosing changes in glacier hydrology from physical principles, using a hydrological model with snow redistribution, sublimation, firnification and energy balance ablation algorithms. *J. Hydrol.*, **608**, 127545, https://doi.org/10.1016/j.jhydrol.2022.127545.

Rood, S. B., J. Pan, K. M. Gill, C. G. Franks, G. M. Samuelson, and A. Shepherd, 2008: Declining summer flows of Rocky Mountain Rivers: Changing seasonal hydrology and probable impacts on floodplain forests. *J. Hydrol.*, **349**, 397–410, https://doi.org/10.1016/j.jhydrol.2007.11.012.

——, G. W. Stupple, and K. M. Gill, 2015: Century-long records reveal slight, ecoregion-localized changes in Athabasca River flows. *Hydrol. Processes*, **29**, 805–816, https://doi.org/10.1002/hyp.10194.

Schindler, D. W., and W. F. Donahue, 2006: An impending water crisis in Canada's western prairie provinces. *Proc. Natl. Acad. Sci. USA*, **103**, 7210–7216, https://doi.org/10.1073/pnas.0601568103.

Shah, M. I., A. Khan, T. A. Akbar, Q. K. Hassan, A. J. Khan, and A. Dewan, 2020: Predicting hydrologic responses to climate changes in highly glacierized and mountainous region Upper Indus basin. *Roy. Soc. Open Sci.*, **7**, 191957, https://doi.org/10.1098/rsos.191957.

Shrestha, N. K., and J. Wang, 2018: Predicting sediment yield and transport dynamics of a cold climate region watershed in changing climate. *Sci. Total Environ.*, **625**, 1030–1045, https://doi.org/10.1016/j.scitotenv.2017.12.347.

——, X. Du, and J. Wang, 2017: Assessing climate change impacts on fresh water resources of the Athabasca River Basin, Canada. *Sci. Total Environ.*, **601–602**, 425–440, https://doi.org/10.1016/j.scitotenv.2017.05.013.

Si, J., and Coauthors, 2023: Effects of climate change on surface runoff and soil moisture in the source region of the Yellow River. *Water*, **15**, 2104, https://doi.org/10.3390/w15122104.

Timoney, K. P., 2021: Flooding in the Peace-Athabasca Delta: Climatic and hydrologic change and variation over the past 120 years. *Climatic Change*, **169**, 34, https://doi.org/10.1007/s10584-021-03257-z.

Torrence, C., and G. P. Compo, 1998: A practical guide to wavelet analysis. *Bull. Amer. Meteor. Soc.*, **79**, 61–78, https://doi.org/10.1175/1520-0477(1998)079<0061:APGTWA>2.0.CO;2.

Wang, C., S. Shang, D. Jia, Y. Han, S. Sauvage, J.-M. Sánchez-Pérez, K. Kuramochi, and R. Hatano, 2018: Integrated effects of land use and topography on streamflow response to precipitation in an agriculture-forest dominated northern watershed. *Water*, **10**, 633, https://doi.org/10.3390/w10050633.

Wolfe, B. B., T. L. Karst-Riddoch, S. R. Vardy, M. D. Falcone, R. I. Hall, and T. W. D. Edwards, 2005: Impacts of climate and river flooding on the hydro-ecology of a floodplain basin, Peace-Athabasca Delta, Canada since AD 1700. *Quat. Res.*, **64**, 147–162, https://doi.org/10.1016/j.yqres.2005.05.001.

Xu, C.-Y., and V. P. Singh, 2004: Review on regional water resources assessment models under stationary and changing climate. *Water Resour. Manage.*, **18**, 591–612, https://doi.org/10.1007/s11269-004-9130-0.

Zaghloul, M. S., E. Ghaderpour, H. Dastour, B. Farjad, A. Gupta, H. Eum, G. Achari, and Q. K. Hassan, 2022: Long term trend analysis of river flow and climate in northern Canada. *Hydrology*, **9**, 197, https://doi.org/10.3390/hydrology9110197.

Zhang, X., K. D. Harvey, W. D. Hogg, and T. R. Yuzyk, 2001: Trends in Canadian streamflow. *Water Resour. Res.*, **37**, 987–998, https://doi.org/10.1029/2000WR900357.